Superconductor Science and Technology

Absence of magnetic interactions in Ni–Nb ferromagnet–superconductor bilayers

To cite this article: Nathan Satchell *et al* 2023 *Supercond. Sci. Technol.* **36** 054002

OPEN ACCESS
IOP Publishing
Superconductor Science and Technology
Supercond. Sci. Technol. **36** (2023) 054002 (9pp)
https://doi.org/10.1088/1361-6668/acc430

Absence of magnetic interactions in Ni–Nb ferromagnet–superconductor bilayers

Nathan Satchell[1,2,*], P Quarterman[3,*], J A Borchers[3], Gavin Burnell[2] and Norman O Birge[1]

[1] Department of Physics and Astronomy, Michigan State University, East Lansing, MI 48824, United States of America
[2] School of Physics and Astronomy, University of Leeds, Leeds LS2 9JT, United Kingdom
[3] NIST Center for Neutron Research, National Institute of Standards and Technology, Gaithersburg, MD 20899, United States of America

E-mail: N.D.Satchell@leeds.ac.uk and patrick.quarterman@gmail.com

Received 27 September 2022, revised 1 March 2023
Accepted for publication 14 March 2023
Published 28 March 2023

Abstract

Studies of ferromagnet-superconductor hybrid systems have uncovered magnetic interactions between the competing electronic orderings. The electromagnetic (EM) proximity effect predicts the formation of a spontaneous vector potential inside a superconductor placed in proximity to a ferromagnet. In this work, we use a Nb superconducting layer and Ni ferromagnetic layer to test for such magnetic interactions. We use the complementary, but independent, techniques of polarized neutron reflectometry and detection Josephson junctions to probe the magnetic response inside the superconducting layer at close to zero applied field. In this condition, Meissner screening is negligible, so our measurements examine only additional magnetic and screening contributions from proximity effects. We report the absence of any signals originating from EM proximity effect in zero applied field. Our observations indicate that either EM proximity effect is below the detection resolution of both of our experiments or may indicate a new phenomenon that requires extension of current theory. From our measurements, we estimate a limit of the size of the zero field EM proximity effect in our Ni–Nb samples to be ± 0.27 mT.

Supplementary material for this article is available online

Keywords: magnetism, superconductivity, Josephson junctions, polarized neutron reflectometry

(Some figures may appear in colour only in the online journal)

* Authors to whom any correspondence should be addressed.

1. Introduction

In the superconducting state, magnetic flux is expelled by the Meissner effect [1]. Hybrid ferromagnet-superconductor (*F*-*S*) systems can exhibit more complex screening properties due to the new physics present at the *F*-*S* interface [2]. Recently, experimental observations via low energy muon spectroscopy reveal an otherwise unexpected contribution to flux expulsion in *F*-*S* bilayers and multilayers below the critical temperature (T_c) of the superconductor [2–6]. In those works Co and Nb are chosen for the *F* and *S* layers respectively. The experimental signature of this effect is an additional screening component originating at the *F*-*S* interface which increases the total flux screening inside the superconductor.

The development of the electromagnetic (EM) proximity effect theory by Mironov *et al* provides a framework in which many of the experimental observations can be interpreted [7]. As a result of the transparency of the *F*-*S* interface, electrons forming Cooper pairs can proximitise the *F* layer. This proximity effect results in many well established transport phenomena, such as π Josephson junctions [8]. Mironov *et al* showed that an added consequence of the proximity effect is that supercurrents flow inside the *F* layer, giving rise to compensating Meissner supercurrents on the superconductor side of the interface. The observable result is a new component of screening at the *F*-*S* interface due to the presence of an additional vector potential.

In the EM proximity effect theory, the additional internal field, B_x, inside the superconductor, at distance x from the *F*-*S* interface, is described as [7],

$$B_x = A_{\mathrm{EM}} e^{-x/\lambda_{\mathrm{L}}}, \tag{1}$$

where A_{EM} is the strength of the EM proximity effect (proportional to the magnetization of the *F* layer) and λ_{L} is the London penetration depth. The key observable predictions of the EM proximity effect are (i) B_x decays with λ_{L}, (ii) A_{EM} oscillates in amplitude and sign with the thickness of the *F* layer, and (iii) A_{EM} (and hence observable B_x) is present even in the absence of an applied magnetic field. The theoretical description of the additional screening currents caused by EM proximity effect is also considered and expanded to structures other than a *F*-*S* bilayer [9–14]. For example, the EM proximity effect also predicts the response of the *F*-*F*-*S* superconducting spin-valve structure [11] studied experimentally [2]. For a review see [15].

Quantitatively, the EM proximity effect theory is applied to model the recent experimental observations of Flokstra *et al* in Co–Nb–Cu trilayers [5]. It is found that Meissner screening alone cannot reproduce the experimental observation of a much enhanced screening in the trilayers compared to Nb and Nb–Cu samples. The depth dependent magnetic signal measured in the muon experiment is then modeled to include both traditional Meissner effect and the additional component of screening predicted by equation (1). The strength of the additional screening component in the Co–Nb–Cu system is found to be $A_{\mathrm{EM}} = -0.9$ mT in a measurement field of 30 mT at 2.5 K.

Other proposed mechanisms for magnetic interactions in *F*-*S* systems include the induced ferromagnetism of Bergeret *et al* [16]. This theory considers a moment at the *F*-*S* interface caused by the local spatial distribution of Cooper pair spins. A number of reports attribute observations to this effect [17–20]. The key observable of Bergeret *et al* is that the induced ferromagnetism decays over the coherence length (ξ), which for thin film Nb is much shorter than λ_L [21–23]. Additionally, spin-triplet pairs can modify the magnetic response of *F*-*S* systems, for example, by introducing a paramagnetic Meissner component [24–29], observed experimentally by the muon technique [30–32].

Considerable research effort has also focused on what we describe here as stray field interactions, where the Meissner effect inside the superconductor acts to screen stray magnetic fields emerging from a ferromagnetic layer. Such stray fields are in some applications considered problematic, for example they can significantly distort the Fraunhofer pattern of ferromagnetic Josephson junctions reducing device functionality [33–35]. It is also possible, however, to engineer structures and devices in which the stray fields provide functionality, such as influencing the ferromagnetic domain structure or providing pinning sites for Abrikosov vortices [36–44].

Additionally, there are several experimental observations of magnetic interactions in *F*-*S* systems where the underlying mechanism either falls outside of the categories outlined previously or remains unexplained [45–50]. For example, a previous report of Flokstra observed a measurable inverse proximity effect in a trilayer sample of Py–Nb–Py by the muon technique, but with a decay length from the *F*-*S* interface much shorter than either ξ or λ_L [45].

In this work, we design and carry out two experiments to test a key prediction of the EM proximity effect: that the induced B_x of equation (1) inside the *S* layer should be present in the absence of applied field. Nb is our superconductor of choice and Ni is chosen as the ferromagnet because (i) it has been extensively studied in Nb–Ni–Nb Josephson junctions [51–60], (ii) the proximity in the Ni–Nb bilayer is expected to be in the clean (ballistic) limit [58], and (iii) the magnetic switching of thin Ni layers is relatively hard compared to the other elemental ferromagnets, such as Co (a requirement of our experiments).

The thickness of the Ni layer is fixed in both experiments at 2.8 nm. This thickness is guided by our preliminary measurements, see supplementary figure S1. In the first experiment, we use polarized neutron reflectometry (PNR) as a sensitive probe of screening and buried interfaces in our Ni–Nb bilayer. Previously, we have used PNR to measure $\lambda_L = 96 \pm 9$ nm (uncertainty represents one standard error) inside a 200 nm thick Nb single layer film in the Meissner state [23]. However, unlike our previous study, here we add the Ni (2.8 nm) layer below the Nb (200 nm) layer. For this experiment we reduce the applied magnetic field as far as possible (while still retaining neutron polarization) so that we are close to zero applied field. Minimizing the applied field has the added benefit of removing contributions to the measured signal from the conventional Meissner effect, which keeps the data interpretation as simple as possible. Any changes in the PNR with the

onset of the superconductivity can thus be attributed to magnetic interactions, such as the profile of equation (1) expected from the EM proximity effect.

Our second experiment uses detection Josephson junctions (DJJs), which are fabricated above Ni–Nb bilayers in direct electronic contact with the Nb following the geometry proposed by Mironov *et al* [7]. We set the Nb thickness here to 90 nm, so that we probe $\approx 1\lambda_L$ ($\approx 8\xi_{GL}$) from the *F*-*S* interface. We fabricate the DJJs with a Ru/Al multilayer barrier, which has a high interfacial resistance and strongly suppresses supercurrent. It is predicted that the EM proximity effect will be observable as a shift in the Fraunhofer pattern of the DJJ from zero applied field [7]. We compare the DJJ samples on the Ni layer to control samples where an insulating layer is placed between the Ni and Nb layers.

We report the absence of any signals originating from EM proximity effect in near-zero applied field. Our observations indicate that either EM proximity effect is below the detection resolution of both of our experiments or may indicate a new phenomenon that requires extension of current theory. For each of our experimental techniques, we calculate upper limits on the size of A_{EM}.

2. Methods

Thin films are deposited by sputtering with base pressure of 2×10^{-8} Torr and partial water pressure of 3×10^{-9} Torr (4×10^{-7} Pa), after liquid nitrogen cooling. We grow the films on 12.5 mm × 12.5 mm Si substrates, which have a typical native oxide layer. Growth is performed at an approximate Ar (6N purity) pressure of 2 mTorr and temperature of −25 °C. Triode sputtering is used for Nb, Ni, and Al from 57 mm diameter targets, and dc magnetron sputtering is used for Au and Ru from 24 mm diameter targets. The targets have 4N purity. Materials are deposited at typical growth rates of 0.4 nm s^{-1} for Nb and Au, and 0.2 nm s^{-1} for Ni, Al, and Ru. Growth rates are calibrated using an *in situ* quartz crystal film thickness monitor and checked by fitting to Kiessig fringes obtained from x-ray reflectometry on reference samples.

For PNR, we grow a series of Ni (2.8)–Nb (200) bilayer sheet films on Si substrates, where the nominal thicknesses are denoted in nanometers. The thickness of the Nb layer is fixed to that of our previous work so that the baseline screening properties are known [23].

For electrical transport samples, we fabricate standard 'sandwich' planer Josephson junctions using methodology described elsewhere [61]. The full structure of the devices is Ni (2.8)–Nb (90)–[Ru (2)–Al (2)]$_6$–Ru (2)–Nb (5)–Au (5)–Nb (150). The Ni–Nb bilayer forms the bottom electrode of our device, where the Nb is chosen to be approximately one penetration depth ($1\lambda_L$) thick. The [Ru–Al]$_6$–Ru multilayer is the barrier for our DJJs and is chosen because the Ru/Al interfaces suppress supercurrent, allowing for tuning of the junctions' critical supercurrent (I_c). In this work, the junctions are circular with a designed diameter of 3 μm and the number of repeats is 6, which suppresses the critical current into the limit where the Josephson penetration depth is much larger than the junction diameter. The Nb (5)–Au (5) capping layers prevent oxidation during lithographic processing. The Nb (150) top electrode is deposited in the final stage of the processing.

Further control samples are fabricated, where the Ni (2.8) layer was replaced by a Ni (2.8)–Nb (5)–Al_2O_3 (2.5) trilayer. The role of the Al_2O_3 insulator is to block any electronic proximity effects for control measurements and the thin non-superconducting Nb layer ensures consistency in the interfacial properties of the Ni layer.

We collect PNR using the Polarized Beam Reflectometer and Multi-Angle Grazing-Incidence K-vector reflectometer at the NIST Center for Neutron Research (NCNR). The incident and scattered neutron spins are polarized parallel or antiparallel to the applied in-plane magnetic field (H) with supermirrors, and reflectivity is measured in the non-spin-flip cross sections ($R^{\uparrow\uparrow}$ and $R^{\downarrow\downarrow}$) as a function of the momentum transfer (Q) normal to the film surface. Given the incident beam is in the grazing configuration for the entire Q range measured, the neutron beam effectively bathes the entire sample, and the data represent an ensemble average. The PNR data are reduced and modeled using the REDUCTUS [62] software package and model-fit using the REFL1D program [63, 64]. The uncertainty of each fitting parameter is estimated using a Markov-chain Monte-Carlo simulation implemented by the DREAM algorithm in the BUMPS Python package [65]. Data are gathered at temperatures as low as 3 K, using a closed cycle refrigerator inserted into a 0.7 T electromagnet with field applied along the substrate orientation.

Electrical transport measurements are performed using a conventional four-point-probe measurement configuration with Keithley 6221 current source and 2182 nanovoltmeter [66]. We collect transport data in a ^{4}He cryostat with variable temperature insert (1.8–300 K) and 3 T superconducting split pair magnet. Magnetic characterization is performed on a Quantum Design MPMS 3 magnetometer [66] on cuttings of sister sheet film samples.

3. Results

3.1. Ferromagnetic and superconducting properties of Ni–Nb bilayers

Figure 1 shows measurements of the sheet film by magnetometry and transport to determine the magnetic switching behavior and onset of superconductivity in our sample. Figure 1(a) shows the in- and out-of-plane magnetic hysteresis loops of the Si(sub)–Ni(2.8)–Nb(200) sample at 10 K. The diamagnetic signal from the substrate has been subtracted. The moment/area is calculated from the measured total moment of the sample and the measured area of the cutting used. The full field range of the acquired data is plotted in the supplementary information.

The in-plane easy axis loop and out-of-plane hard axis loop of figure 1(a) indicate that the Ni has the expected in-plane magnetization. For in-plane applied fields, the Ni layer has a remanence of ≈75%, a coercive field of ≈16 mT, and a saturation field of ≈200 mT. The reduction of the remanence from 100% and the large saturation field are suggestive that

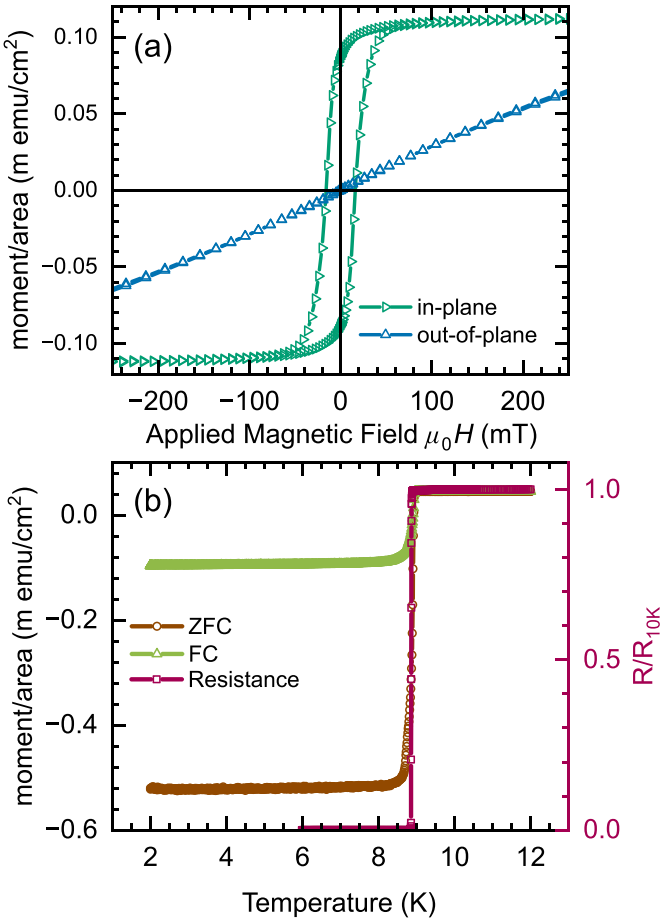

Figure 1. Magnetic and transport characterization of the Si(sub)–Ni(2.8)–Nb(200) film sample. (a) Magnetic hysteresis loops acquired at a temperature of 10 K with the applied field oriented in-plane and out-of-plane. The diamagnetic contribution from the substrate has been subtracted. Moment/area is calculated from the measured total moment and the measured area of the sample cutting. (b) Left axis: moment versus temperature in an in-plane applied field of 1 mT in the zero field cooled (ZFC) and field cooled (FC) conditions. The temperature dependent signal is due to Nb screening the field. Right axis: normalized resistance versus temperature. The T_c of the sample from these measurements is taken either at the onset of the screening signal or the reduction in electrical resistivity to 50% the normal state value and is 8.93 ± 0.03 K (uncertainty represents one standard error). Lines connecting the data points are guides.

the Ni forms a multidomain structure when the applied field is removed. The volume magnetization of the sample at saturation is calculated from the nominal thickness of the Ni layer to be 400 ± 40 emu cm^{-3} (1 emu cm^{-3} = 1 kA m^{-1}) (uncertainty represents one standard error), which is lower than the expected value of 485 emu cm^{-3}. We attribute the lower volume magnetization of our sample to the formation of magnetic dead layers, which we estimate from the reduction in the measured volume magnetization from the bulk value to have a thickness of 0.5 nm in our sample. The PNR results presented in section 3.2 and table 1 confirm the presence of a magnetic dead layer in the sample at the SiO_x/Ni interface.

Figure 1(b) shows the moment versus temperature of the sample on the left axis obtained at 1 mT in-plane measurement field in the zero field cooled and field cooled conditions. At 1 mT in-plane field, the Ni is close to the remanent state and will be the major contribution to the signal above the T_c of Nb. In the range of temperatures from 2–12 K the magnetization of the Ni is not expected to change, so we attribute the temperature dependent signal to the onset of superconductivity in the Nb layer. Plotted on the right axis is the normalized resistance of the sample. The T_c of the sample from these measurements is taken either at the onset of the screening signal or the reduction in electrical resistivity to 50% of the normal state value and is 8.93 ± 0.03 K (uncertainty represents one standard error). This is a slight reduction from a comparable single Nb layer (9.10 ± 0.05 K [23]). The full temperature range of the acquired transport data is plotted in the supplementary information.

3.2. Polarized neutron reflectometry

We perform PNR at as close to zero applied field as possible. In PNR, a small guide field is needed to maintain beam polarization. The smallest possible applied field is found to be 1 mT, and is hence used as our measurement field. To limit concerns of flux trapping in the sample, we do not change field when below the transition temperature of the Nb (9 K). When changing field states, the temperature is increased to approximately 20 K. For reproducibility of the magnetic field condition, a saturating field of 700 mT is then applied, followed by lowering to the 1 mT guide field, and finally the sample is either measured at 20 K to provide the normal state condition or is cooled to the base temperature of 3 K in the superconducting state.

Figure 2(a) shows the non-spin-flip cross-section PNR in the normal state (20 K) and the best fit to the reflectivity. At 20 K, the only expected magnetic contribution in the sample is the magnetization of the Ni layer. To fully describe the reflectivity, a structural multilayer model is constructed, where each layer in the model has a thickness, roughness, and scattering length density fit parameter. Additionally, the magnetic scattering length density is fitted for the Ni layer. The best fit to the model is shown in figure 2(a), where the structural and magnetic scattering length density depth profile corresponding to the model are given in figure 2(b) and the best fit parameters in table 1.

Modeling the 20 K data provides the following insights to our sample. The fitted layer thicknesses are close to the nominal growth thicknesses. At 20 K, the only magnetic contribution in the sample comes from the Ni layer with zero moment in the rest of the sample. The fitted magnetic dead layer thicknesses of 0.4 nm at the SiO_x/Ni interface and 0.0 nm at the Ni/Nb interface are consistent with the estimated dead layer thickness from magnetometry presented in section 3.1.

Figures 2(c) and (d) show the main results of our PNR investigation into the EM proximity effect. The spin asymmetry $[SA = (R^{\uparrow\uparrow} - R^{\downarrow\downarrow})/(R^{\uparrow\uparrow} + R^{\downarrow\downarrow})]$ for the Si(sub)–Ni(2.8)–Nb(200) film sample at an applied field of 1 mT and temperatures of 20 and 3 K are shown in figure 2(c). In both the normal (20 K) and superconducting (3 K) states, there is zero spin asymmetry below the critical edge of the reflectivity, followed by an increasingly positive spin asymmetry with

Table 1. Best fit parameters corresponding to the 20 K PNR model shown in figure 2. The uncertainty of each fitting parameter is estimated using the DREAM algorithm, see text.

Layer	Thickness nm	Roughness nm	Nuclear SLD 10^{-6} Å^{-2}	Magnetic SLD 10^{-6} Å^{-2} (emu cm^{-3})
Nb	195.3 ± 0.2	3.0 ± 0.1	4.07 ± 0.02	0
Ni	2.7 ± 0.2	0.8 ± 0.2	9.5 ± 0.1	0.9 ± 0.1 (320 ± 30)
Ni (dead layer)	0.4 ± 0.25		9.5 ± 0.1	0
SiO_x	3.3 ± 0.25	1.7 ± 0.3	3.6 ± 0.3	0
Si		0.5	2.069	0

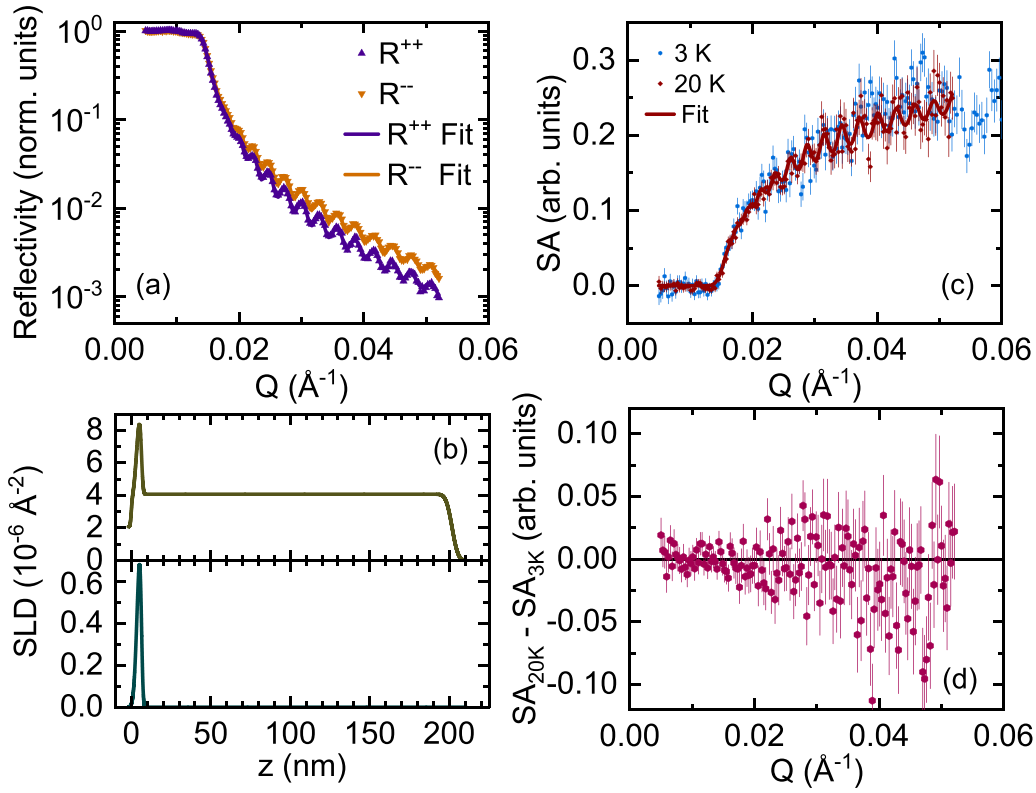

Figure 2. Polarized neutron reflectometry measurements of the Si(sub)–Ni(2.8)–Nb(200) film sample at an applied field of 1 mT. (a) Non-spin-flip cross-section PNR data (points) with theoretical fits (line) at 20 K. (b) Nuclear (yellow, top) and magnetic (green, bottom) scattering length densities corresponding to the theoretical fits shown in (a). The best fit parameters are given in table 1. $Z = 0$ refers to the Si substrate surface. (c) The spin asymmetry at 20 K (red) and 3 K (blue). (d) The changes in the spin asymmetry between 20 K and 3 K. A horizontal line at $SA_{20K} - SA_{3K} = 0$ is included to indicate to the reader that there are no significant changes to the PNR signal when the sample is cooled into the superconducting state. Presented uncertainties represent one standard error.

an oscillation. As expected, the fit corresponding to the structural and magnetic profile of figure 2(b) describes the spin-asymmetry well.

At 3 K, magnetic contributions from the superconducting state are expected in addition to that of the Ni layer. As we demonstrate in the supplementary information (figure S2), at the 1 mT applied field, the Meissner contribution is too small to influence the PNR data in a measurable way. Therefore, when entering the superconducting state, only contributions from magnetic interactions, including the expected profile of equation (1), influence the PNR.

The key result of our PNR study is that comparing the measured spin asymmetry above and below the superconducting T_c, we observe no systematic changes with the onset of superconductivity. To be clear, the PNR data show no evidence of a magnetic proximity effect in near-zero field. That result is highlighted in figure 2(d), where we plot the difference in spin asymmetry ($SA_{20K} - SA_{3K}$). The only deviations from $SA_{20K} - SA_{3K} = 0$ are the scatter of individual data points. Such differences are not consistent with simulations of either a Meissner screening profile, equation (1), or a combination of both. To confirm whether our data set is consistent with $SA_{20K} - SA_{3K} = 0$, we perform a χ^2 analysis relative to zero. The returned $\chi^2 = 175.15$ for 157 data points suggests that the difference in our data is indistinguishable from zero with $\approx 2\sigma$ confidence level. In a restricted region near the critical angle from $Q = 0.012$ to 0.022 Å^{-1} where the difference should be most pronounced, the calculated $\chi^2 = 24.7$ for 34 data points, which gives a reduced χ^2 smaller than 1.

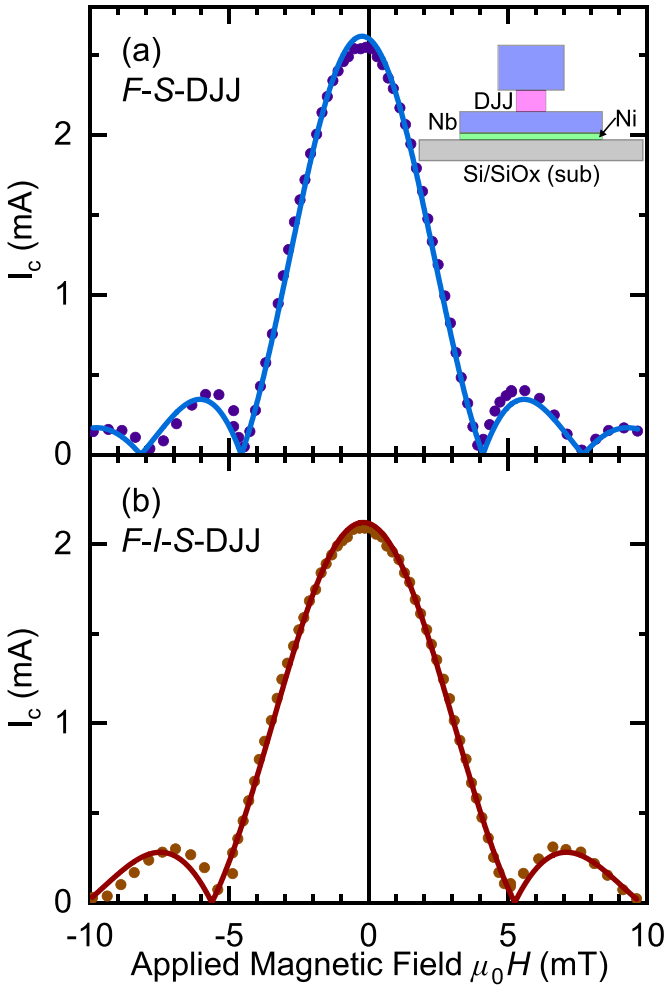

Figure 3. Representative $I_c(B)$ Fraunhofer patterns for the DJJ devices at 1.8 K. (a) The DJJ is placed on a Ni (2.8)–Nb (90) bilayer. (b) A control sample where an Al_2O_3 (2.5 nm) insulator layer is added between the Ni and Nb. The error in determining I_c is smaller than the data points. Solid lines show fit to equations (2) and (3) to extract $H_{\rm shift}$, the amount the Fraunhofer pattern is shifted from zero applied field. Both devices show a small negative $H_{\rm shift}$.

3.3. Detection Josephson junctions

DJJs are fabricated above the Ni (2.8)–Nb (90) bilayer. The geometry of the devices is shown in the inset of figure 3(a) and our DJJs are designed to closely follow the devices theoretically proposed to measure the EM proximity effect in [7]. The design width of the bottom electrode, containing the Ni/Nb bilayer, is 18 μm. The length of the bottom electrode is 2400 μm and six DJJs are placed along the length of the bottom electrode with design widths of 3 μm. In-plane magnetic fields are applied along the long axis of the bottom electrode.

Figure 3 shows representative $I_c(B)$ Fraunhofer response of our DJJs. The Fraunhofer patterns of two samples are presented. In the first sample, the superconducting Nb layer is in direct electronic contact with the Ni layer. In the second control sample, the Nb layer is separated from the Ni layer by a dielectric Al_2O_3 layer, which removes any electronic proximity effects. For circular Josephson junctions, the I_c(B) response can be described by the Airy function [67],

$$I_c = I_{c0}\,|2J_1(\pi\,\Phi\,/\Phi_0)/(\pi\,\Phi\,/\Phi_0)|\,, \tag{2}$$

where I_{c0} is the maximum critical current, J_1 is a Bessel function of the first kind, $\Phi_0 = h/2e$ is the flux quantum, and Φ is the flux through the junction. In our case,

$$\Phi = \mu_0(H_{\rm app} - H_{\rm shift})w(2\lambda_{\rm L} + d), \tag{3}$$

where w, $\lambda_{\rm L}$ and d are the width of the junction, the effective London penetration depth of the electrodes [67], and the total thickness of all the normal metal layers and F layers in the junction. $H_{\rm app}$ is the applied field and $H_{\rm shift}$ is the key parameter we report here, the amount I_{c0} is shifted from $H = 0$. We expect that $H_{\rm shift}$ corresponds to the condition when the external applied field cancels the internal field from the EM proximity effect (B_x) at the junction, $\mu_0 H_{\rm shift} = -B_x$.

For consistency, prior to each measurement we follow the following initialization routine. The samples are first held above the T_c of Nb at 12 K and magnetized with an in-plane applied field of +1 T to fully saturate the Ni layer. The field is applied in the long axis of the device's bottom electrode. The saturation field is removed and we cool the sample in zero applied field (in practice there will inevitably be a small remanent field due to trapped flux in the magnet). Once the temperature reaches 1.8 K (the base temperature of our cryostat), the samples are measured by recording the $I-V$ characteristic to extract $I_c(B)$ at each applied field in the range 10 to −10 mT. After the measurement sequence is complete, the sample is warmed to 12 K and we repeat the cycle.

The $I_c(B)$ Fraunhofer measurements shown in figure 3 are representative examples of $I_c(B)$ device behavior. We performed multiple measurements on a total of six devices (3 F-S and 3 F-I-S control samples) to calculate average values of $\overline{H}_{\rm shift}$. For the F-S devices, $\mu_0\overline{H}_{\rm shift} = -0.26 \pm 0.02$ mT. For the F-I-S control devices, $\mu_0\overline{H}_{\rm shift} = -0.23 \pm 0.03$ mT. Therefore, although we do observe that $\mu_0\overline{H}_{\rm shift} \neq 0$, there is not an obvious signal attributable to the EM proximity effect as the $\mu_0\overline{H}_{\rm shift}$ is observed in the control samples also.

There are two potential sources of the observed non-zero $\overline{H}_{\rm shift}$ in our experiment which would be expected to be present for both the F-S and F-I-S control samples. The first is trapped flux in the superconducting coils which apply the measurement field. To explore this contribution, we measure identical DJJ device without the Ni layer. Any $H_{\rm shift}$ observed in the sample without the Ni layer is related to the trapped flux in our superconducting coils. As shown in supplemental figure S4, the observed $\mu_0 H_{\rm shift} = 0.15$ mT indicates that a small positive applied field must be applied to cancel the trapped flux and achieve the zero field condition. Interestingly, the direction of $H_{\rm shift}$ observed in the sample without the Ni layer is opposite to the direction of $H_{\rm shift}$ observed in the devices with the Ni layer.

A second possible source of non-zero $\overline{H}_{\rm shift}$ are stray fields from the Ni layer. There are many possible sources of stray fields from the Ni layer including any combination of return fields, the edges of the devices, domain walls, and orange peel roughness [68]. We believe that stray fields are the most likely source of our observed small negative $\overline{H}_{\rm shift}$.

The differences in the $I_c(B)$ and width of the central lobe of the Fraunhofer patterns of the two presented devices shown in figures 3(a) and (b) are due to the sample to sample variation in defining the diameter of the DJJ by photolithography. The fitted diameter of the *F-S* sample is 2.9 μm and the *F-I-S* control sample is 2.3 μm.

4. Discussion

PNR simulations of equation (1) applied to our Ni–Nb bilayer imply that changes in the sample magnetization or excluded magnetic field due to the EM proximity effect should manifest in the spin asymmetry, as this quantity is sensitive to the magnetic induction in the sample. By comparing the fidelity of our experimental data in figure 2 to the results of these simulations, we do not see any evidence of additional magnetism from proximity effects but can estimate an approximate limit on the size of $A_{\rm EM}$ at zero applied field. First we note that the field expulsion expected with a London penetration depth of 96.2 nm from the Meissner effect [23] at 3 K in a 1 mT field does not detectably alter the model for the reflectivity and spin asymmetry. (As shown in supplementary figures S2 and S3, this behavior contrasts with that observed in a larger field of 150 mT.) Next we consider the variation in the spin asymmetry that is expected if $A_{EM} = \pm 0.9$ mT, which matches the magnitude of the effect observed by Flokstra *et al* in Co (2.4)–Nb bilayers [5]. As a reminder, A_{EM} in equation (1) is proportional to the Ni magnetization in our case, which was determined from the PNR fit shown in figures 2(a) and (c) to be 317 emu cm^{-3} (table 1) in the 1 mT remanent field. As seen in figure 4, the models for these values of A_{EM} deviate substantially from the 3 K PNR spin asymmetry data, especially in the region near the critical angle. The magnitude of A_{EM} was gradually decreased in order to approximate the sensitivity of the PNR measurement. Figure 4 shows the model fits calculated for $A_{EM} = \pm$ 0.27 mT, which seem to be just above the detection limit for this technique.

The Josephson junction experiment can also be used to estimate the limit of the EM proximity effect and the parameter $A_{\rm EM}$. The Fraunhofer pattern of the DJJ is centered where the total field in the junction is zero. Assuming no stray fields or trapped flux, in the presence of the EM proximity effect the total field in the DJJ will be zero when the external applied field cancels the internal field of the EM proximity effect, which from equations (1) and (3) is the condition $\mu_0 H_{\rm shift} = -B_x$. If $\mu_0 H_{\rm shift} = 0$, we can estimate the limit of $A_{\rm EM}$ from the experimental uncertainty in determining $\mu_0 H_{\rm shift}$. In our experiment, due to the presence of stray fields and/or trapped flux, $\mu_0 H_{\rm shift} \neq 0$ for either the *F-S* or *F-I-S* control samples. In this case, it is the difference in $\mu_0 \overline{H}_{\rm shift}$ between the two sample geometries which provides B_x and hence $A_{\rm EM}$. The experimental uncertainty in determining $\mu_0 \overline{H}_{\rm shift}$ from the *F-S* DJJ devices is ± 0.02 mT and from the *F-I-S* control samples is ± 0.03 mT. Therefore, it is reasonable to expect to be able to observe changes in $\mu_0 \overline{H}_{\rm shift}$ between the sample geometries that are of the order ± 0.1 mT. A difference of ± 0.1 mT would correspond to $A_{\rm EM}$ at the Ni–Nb interface of ± 0.27 mT, which we conclude from both the DJJ and PNR techniques to be the upper limit of the EM proximity effect at zero applied field in our samples.

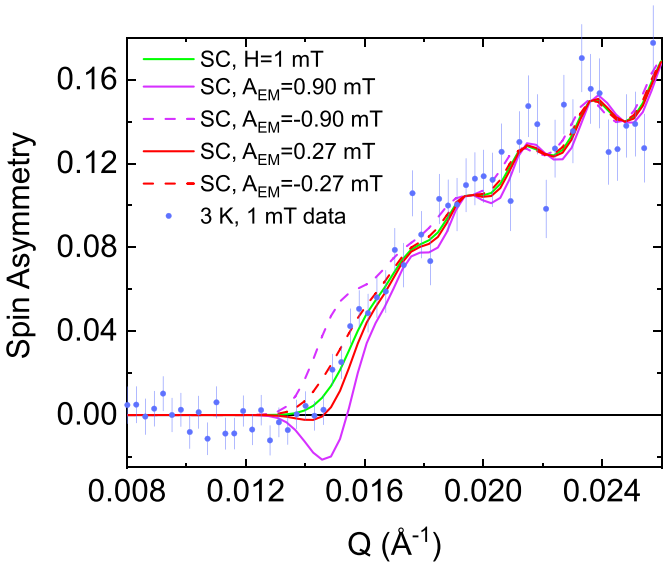

Figure 4. The spin asymmetry of the Si(sub)–Ni(2.8)–Nb(200) film at 3 K (color circles) with model fits assuming superconductivity with a London penetration depth of 96.2 nm in a 1 mT field. The effects of an additional proximity effect are considered for $A_{EM} = \pm 0.27$ mT (solid and dashed color lines) as well as ± 0.9 mT (solid and dashed color lines). Presented uncertainties represent one standard error.

The absence of detectable $A_{\rm EM}$ in the PNR and DJJ measurements suggests that any signals of the EM proximity effect at zero applied field are below the observable limit resolution of our presented measurements, which we estimate to be $A_{\rm EM} < \pm 0.27$ mT. By comparison to this limit, Flokstra *et al* report $A_{\rm EM} = -0.9$ mT in Co (2.4)–Nb bilayers by the muon technique [5]. An $A_{\rm EM}$ of this magnitude, if present in our samples, should be observable in both of our experiments.

Alternatively, the absence of detectable $A_{\rm EM}$ in our experiments may indicate a new phenomenon that requires extension of current theory. An important difference between the experimental results we report in this work and the previous *F-S* experimental works using the muon technique is the coexistence of conventional screening currents in those previous works. In the muon technique, the measurements are performed in an applied magnetic field, typically 10–40 mT, and the reported observations of *F-S* proximity effect manifests as a modification of the conventional Meissner screening [2–6, 30–32]. Our observations may imply that the expected EM proximity effect manifests only when there are coexisting screening currents, and not in the zero field condition of this work. The zero field muon experiment has not been attempted, but the applied field dependence of the excess screening reported by Flokstra *et al* may support such conclusions [3].

High field measurements using the DJJs are not possible due to the Fraunhofer physics of the junction. On the other hand, PNR can be performed at high field and exploratory measurements in an applied field of 150 mT are reported in

supplemental figure S3. The PNR at 150 mT shows a pronounced difference upon entering the superconducting state for our sample with the Ni adjacent to the Nb layer and for a second sample with the Ni and Nb separated with an insulating spacer layer. The Ni–Nb data are not well described by a model accounting for only simple Meissner screening in the superconducting state. We present a fit to the Ni–Nb data with a linear combination of the Meissner and EM proximity formalisms in the superconducting state, which is not inconsistent with a finite A_{EM}. However, to fully describe the data, a model accounting for vortices is required.

The observation in our DJJ experiments of $\overline{H}_{\mathrm{shift}}$ in both our proximity samples and control samples (in which the proximity effect is suppressed by the addition of an insulating layer) highlights the importance of control experiments in this field.

5. Conclusions

In conclusion, we have performed PNR and DJJ measurements on a bilayer sample of Ni(2.8 nm)/Nb. Our measurements probe for additional contributions to the screening and magnetization of the samples below the superconducting transition temperature at close to zero applied field. We report the absence of any signals originating from EM proximity effect in zero applied field. Our observations indicate that either EM proximity effect is below the detection resolution of both of our experiments or may indicate a new phenomenon that requires extension of current theory. From our measurements, we estimate a limit of the size of the zero field EM proximity effect in our Ni–Nb samples to be ± 0.27 mT.

The data associated with this paper are openly available from the NCNR and University of Leeds data repositories [69].

Data availability statement

The data that support the findings of this study are openly available at the following URL/DOI: https://doi.org/10.5518/1245 [69].

Acknowledgments

We are grateful to Brian J. Kirby for helpful, in-depth discussions. We acknowledge the support of the EPSRC through Grant No. EP/V028138/1. PQ acknowledges support from the National Research Council Research Associateship Program. This project has received partial funding from the European Unions Horizon 2020 research and innovation programme under the Marie Skłodowska-Curie Grant Agreement No. 743791 (SUPERSPIN).

ORCID iDs

Nathan Satchell https://orcid.org/0000-0003-1597-2489
P Quarterman https://orcid.org/0000-0001-6272-6243
J A Borchers https://orcid.org/0000-0002-3348-8212
Gavin Burnell https://orcid.org/0000-0002-9486-0639
Norman O Birge https://orcid.org/0000-0001-7840-3908

References

[1] Meissner W and Ochsenfeld R 1933 *Naturwissenschaften* **21** 787
[2] Flokstra M G *et al* 2016 *Nat. Phys.* **12** 57–61
[3] Flokstra M G, Stewart R, Satchell N, Burnell G, Luetkens H, Proksch T, Suter A, Morenzoni E, Langridge S and Lee S L 2018 *Phys. Rev. Lett.* **120** 247001
[4] Stewart R *et al* 2019 *Phys. Rev.* B **100** 020505
[5] Flokstra M G, Stewart R, Satchell N, Burnell G, Luetkens H, Proksch T, Suter A, Morenzoni E, Langridge S and Lee S L 2019 *Appl. Phys. Lett.* **115** 072602
[6] Flokstra M G, Stewart R, Satchell N, Burnell G, Luetkens H, Proksch T, Suter A, Morenzoni E and Lee S L 2021 *Phys. Rev.* B **104** L060506
[7] Mironov S, Mel'nikov A S and Buzdin A 2018 *Appl. Phys. Lett.* **113** 022601
[8] Buzdin A I 2005 *Rev. Mod. Phys.* **77** 935–76
[9] Bergeret F S, Volkov A F and Efetov K B 2001 *Phys. Rev.* B **64** 134506
[10] Volkov A F, Bergeret F S and Efetov K B 2019 *Phys. Rev.* B **99** 144506
[11] Devizorova Z, Mironov S V, Mel'nikov A S and Buzdin A 2019 *Phys. Rev.* B **99** 104519
[12] Dahir S M, Volkov A F and Eremin I M 2019 *Phys. Rev.* B **100** 134513
[13] Bespalov A 2022 *Physica* C **595** 1354032
[14] Putilov A V, Mironov S V, Mel'nikov A S and Buzdin A I 2022 *Phys. Rev.* B **105** 064510
[15] Mironov S V, Samokhvalov A V, Buzdin A I and Mel'nikov A 2021 *JETP Lett.* **113** 92–101
[16] Bergeret F S, Volkov A F and Efetov K B 2004 *Phys. Rev.* B **69** 174504
[17] Salikhov R I, Garifullin I A, Garif'yanov N N, Tagirov L R, Theis-Bröhl K, Westerholt K and Zabel H 2009 *Phys. Rev. Lett.* **102** 087003
[18] Xia J, Shelukhin V, Karpovski M, Kapitulnik A and Palevski A 2009 *Phys. Rev. Lett.* **102** 087004
[19] Khaydukov Y N, Aksenov V, Nikitenko Y V, Zhernenkov K, Nagy B, Teichert A, Steitz R, Rühm A and Bottyán L 2011 *J. Supercond. Nov. Magn.* **24** 961–8
[20] Khaydukov Y N *et al* 2013 *JETP Lett.* **98** 107–10
[21] Zhang H, Lynn J W, Majkrzak C F, Satija S K, Kang J H and Wu X D 1995 *Phys. Rev.* B **52** 10395–404
[22] Gubin A I, Il'in K S, Vitusevich S A, Siegel M and Klein N 2005 *Phys. Rev.* B **72** 064503
[23] Quarterman P, Satchell N, Kirby B J, Loloee R, Burnell G, Birge N O and Borchers J A 2020 *Phys. Rev. Mater.* **4** 074801
[24] Löfwander T, Champel T, Durst J and Eschrig M 2005 *Phys. Rev. Lett.* **95** 187003
[25] Bergeret F S and García N 2004 *Phys. Rev.* B **70** 052507
[26] Yokoyama T, Tanaka Y and Nagaosa N 2011 *Phys. Rev. Lett.* **106** 246601
[27] Mironov S, Mel'nikov A and Buzdin A 2012 *Phys. Rev. Lett.* **109** 237002
[28] Alidoust M, Halterman K and Linder J 2014 *Phys. Rev.* B **89** 054508
[29] Espedal C, Yokoyama T and Linder J 2016 *Phys. Rev. Lett.* **116** 127002
[30] Di Bernardo A *et al* 2015 *Phys. Rev.* X **5** 041021
[31] Rogers M *et al* 2021 *Commun. Phys.* **4** 1–9
[32] Alpern H *et al* 2021 *Phys. Rev. Mater.* **5** 114801
[33] Bourgeois O, Gandit P, Lesueur J, Sulpice A, Grison X and Chaussy J 2001 *Eur. Phys. J.* B **21** 75–80

[34] Khaire T S, Pratt W P and Birge N O 2009 *Phys. Rev.* B **79** 094523
[35] Khasawneh M A, Pratt W P and Birge N O 2009 *Phys. Rev.* B **80** 020506
[36] Tamegai T, Nakao Y, Mohan S and Nakajima Y 2011 *Supercond. Sci. Technol.* **24** 024015
[37] Curran P J *et al* 2015 *Appl. Phys. Lett.* **107** 262602
[38] Del Valle J, Gomez A, Gonzalez E, Osorio M, Granados D and Vicent J 2015 *Sci. Rep.* **5** 1–7
[39] Vlasko-Vlasov V K, Colauto F, Buzdin A I, Rosenmann D, Benseman T and Kwok W-K 2017 *Phys. Rev.* B **95** 144504
[40] Curran P, Kim J, Satchell N, Witt J, Burnell G, Flokstra M G, Lee S L and Bending S 2017 *Appl. Phys. Lett.* **110** 262601
[41] Marchiori E, Curran P J, Kim J, Satchell N, Burnell G and Bending S J 2017 *Sci. Rep.* **7** 45182
[42] Patiño E J and Blamire M G 2018 *Supercond. Sci. Technol.* **32** 01LT02
[43] Satchell N 2019 *Supercond. Sci. Technol.* **32** 020501
[44] Wang Y-L, Ma X, Xu J, Xiao Z-L, Snezhko A, Divan R, Ocola L E, Pearson J E, Janko B and Kwok W-K 2018 *Nat. Nanotechnol.* **13** 560–5
[45] Flokstra M G, Ray S J, Lister S J, Aarts J, Luetkens H, Prokscha T, Suter A, Morenzoni E and Lee S L 2014 *Phys. Rev.* B **89** 054510
[46] Hernández U D C, Fontes M B, Baggio-Saitovitch E, Sousa M A and Enderlein C 2017 *Phys. Rev.* B **95** 184509
[47] Khaydukov Y N, Kravtsov E A, Zhaketov V D, Progliado V V, Kim G, Nikitenko Y V, Keller T, Ustinov V V, Aksenov V L and Keimer B 2019 *Phys. Rev.* B **99** 140503
[48] Satariano R *et al* 2021 *Phys. Rev.* B **103** 224521
[49] Satariano R *et al* 2022 *IEEE Trans. Appl. Supercond.* **32** 1–5
[50] Nagy B *et al* 2016 *Europhys. Lett.* **116** 17005
[51] Blum Y, Tsukernik A, Karpovski M and Palevski A 2002 *Phys. Rev. Lett.* **89** 187004
[52] Shelukhin V *et al* 2006 *Phys. Rev.* B **73** 174506
[53] Robinson J W A, Piano S, Burnell G, Bell C and Blamire M G 2006 *Phys. Rev. Lett.* **97** 177003
[54] Robinson J W A, Piano S, Burnell G, Bell C and Blamire M G 2007 *Phys. Rev.* B **76** 094522
[55] Robinson J W A, Piano S, Burnell G, Bell C and Blamire M G 2007 *IEEE Trans. Appl. Supercond.* **17** 641–4
[56] Bannykh A A, Pfeiffer J, Stolyarov V S, Batov I E, Ryazanov V V and Weides M 2009 *Phys. Rev.* B **79** 054501
[57] Baek B, Rippard W H, Benz S P, Russek S E and Dresselhaus P D 2014 *Nat. Commun.* **5** 3888
[58] Baek B, Schneider M L, Pufall M R and Rippard W H 2017 *Phys. Rev. Appl.* **7** 064013
[59] Baek B, Schneider M L, Pufall M R and Rippard W H 2018 *IEEE Trans. Appl. Supercond.* **28** 1800705
[60] Tolpygo S K, Bolkhovsky V, Rastogi R, Zarr S, Day A L, Golden E, Weir T J, Wynn A and Johnson L M 2019 *IEEE Trans. Appl. Supercond.* **29** 1101208
[61] Wang Y, Pratt W P and Birge N O 2012 *Phys. Rev.* B **85** 214522
[62] Maranville B, Ratcliff I I W and Kienzle P 2018 *J. Appl. Crystallogr.* **51** 1500–6
[63] Kirby B J, Kienzle P A, Maranville B B, Berk N F, Krycka J, Heinrich F and Majkrzak C F 2012 *Curr. Opin. Colloid Interface Sci.* **17** 44–53
[64] Kienzle P, Maranville B B and Kirby B 2017 Reflectometry software (available at: www.nist.gov/ncnr/data-reduction-analysis/reflectometry-software)
[65] JCGM 2008 *International organization for standardization, guide to the expression of uncertainty in measurement* (available at: www.bipm.org/utils/common/documents/jcgm/JCGM_100_2008_E.pdf)
[66] Certain commercial products or company names are identified here to describe our study adequately. Such identification is not intended to imply recommendation or endorsement by the National Institute of Standards and Technology, nor is it intended to imply that the products or names identified are necessarily the best available for the purpose
[67] Barone A and Paterno G 1982 *Physics and Applications of the Josephson Effect* (New York: Wiley)
[68] Schrag B *et al* 2000 *Appl. Phys. Lett.* **77** 2373–5
[69] Satchell N, Quarterman P, Borchers J A, Burnell G and Birge N O 2023 Absence of magnetic interactions in Ni–Nb ferromagnet–superconductor bilayers *Dataset* (University of Leeds) (https://doi.org/10.5518/1245)